

See discussions, stats, and author profiles for this publication at: <https://www.researchgate.net/publication/235764858>

Thermal Diffusion at Nanoscale: From CoAu Alloy Nanoparticles to Co@Au Core/Shell Structures

ARTICLE *in* THE JOURNAL OF PHYSICAL CHEMISTRY C · JANUARY 2013

Impact Factor: 4.77 · DOI: 10.1021/jp310971f

CITATIONS

11

READS

77

8 AUTHORS, INCLUDING:



Lidia Martínez

Spanish National Research Council

37 PUBLICATIONS 279 CITATIONS

SEE PROFILE



Carmen Ballesteros

University Carlos III de Madrid

155 PUBLICATIONS 1,507 CITATIONS

SEE PROFILE



Yves Huttel

Instituto de Ciencia de Materiales de Madrid

83 PUBLICATIONS 825 CITATIONS

SEE PROFILE

Thermal Diffusion at Nanoscale: From CoAu Alloy Nanoparticles to Co@Au Core/Shell Structures

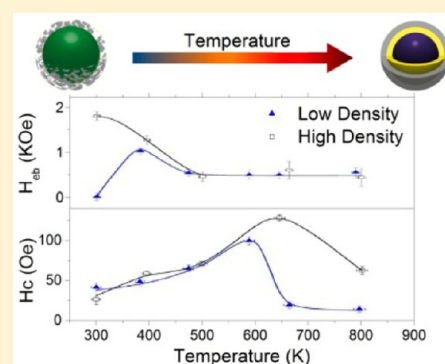
D. Llamosa Pérez,[†] A. Espinosa,[†] L. Martínez,[†] E. Román,[†] C. Ballesteros,[‡] A. Mayoral,[§] M. García-Hernández,[†] and Y. Huttel^{*,†}

[†]Instituto de Ciencia de Materiales de Madrid (ICMM-CSIC), c/Sor Juana Inés de la Cruz, 3, 28049 Cantoblanco, Madrid, Spain

[‡]Departamento de Física, EPS, Universidad Carlos III, 28911 Madrid, Spain

[§]Laboratorio de Microscopías Avanzadas (LMA), Instituto de Nanociencia de Aragón (INA), Universidad de Zaragoza, c/Mariano Esquillor, Edificio I+D, 50018 Zaragoza, Spain

ABSTRACT: The thermal-induced diffusion at nanoscale is investigated through the detailed study of the structural and magnetic properties of Co@Au nanoparticles as a function of the deposition temperature. Nanoparticles of 10 nm were fabricated using an ion cluster source from a Co₉₅Au₅ target. While low-temperature deposition leads to the formation of an alloyed fcc CoAu core with an incomplete cobalt oxide shell, higher deposition temperature induces the formation of a pure hcp Co core with an intermediate Au shell and a compact outer cobalt oxide shell. The evolution of the magnetic properties of the nanoparticles is presented and discussed in light of the structural changes of the nanoparticles upon deposition temperature and nanoparticle density. It is found that thermal-induced diffusion can be successfully used to tune the structural and magnetic properties at the nanoscale in CoAu nanoparticles.



1. INTRODUCTION

The fundamental properties of objects at the nanoscale level are unique and significantly different as compared to bulk or single atoms. Over the last decades, significant effort has been devoted to the production and understanding of nanomaterials.^{1–3} In the case of nanoparticles made of magnetic compounds, it is well-known that by decreasing the particle size the magnetic anisotropy energy per particle responsible for holding the magnetic moment along certain directions becomes comparable to the thermal energy. Below a critical size, the thermal fluctuations induce random flipping of the magnetic moment with time, and the nanoparticles lose their stable magnetic order, becoming superparamagnetic. Thus, the demand for further miniaturization comes into conflict with the superparamagnetism caused by the reduction of the anisotropy energy per particle: this constitutes the so-called “superparamagnetic limit”.⁴

One way to reduce the particle size without losing the magnetic isotropy is to introduce an extra energy called Exchange Bias (EB). Particular attention has been paid to core@shell nanoparticles (CSNPs) as a possible alternative to beat the superparamagnetic limit. In this way, NPs made of a ferromagnetic (FM) core and an oxide shell that is usually an antiferromagnet (AF) are of special interest. It is well-known that the proximity of a FM and an AF induces an exchange anisotropy at the interface that is the EB.⁵ This EB produces a shift of the hysteresis loop after cooling in the presence of a magnetic field and is defined as the EB field, H_{eb} . The EB is usually described as an additional unidirectional anisotropy. It

has been reported that the increase in coercivity induced by the exchange coupling can lead to a substantial increase in the stability of the ferromagnetic clusters, which results in a suppression of the superparamagnetic fluctuations below the Néel temperature.^{4,6}

Another approach consists in fabricating “free” CSNPs (i.e., not embedded into a matrix) that do not exhibit EB and are made of a ferromagnetic core and a protective shell that avoids the degradation of the ferromagnetic core and its magnetic properties. Within such an approach, the core size needs to be slightly bigger than the superparamagnetic limit size, and it can never be smaller as it occurs in the case of systems that exhibit EB. Moreover, the protective shell has to be continuous to fully protect the ferromagnetic core against oxidation or any degradation from the surrounding media. Additionally, the protective shell cannot intermix with the ferromagnetic core since such intermixing would induce an effective ferromagnetic size reduction and the loss of ferromagnetic behavior. Many CSNPs have been reported in the literature with different shells that include oxide shells^{7–10} but also nonoxide shells.^{11–15} The coating of cobalt nanoparticles with an appropriate shell is likely to overcome the oxidation (and hence deterioration of the magnetic properties) and poor biocompatibility. Therefore, efforts have been made in creating biocompatible cobalt nanoparticles by growing a gold shell.¹⁶ On the other hand, it

Received: November 6, 2012

Revised: January 17, 2013

Published: January 21, 2013

should be noted that the use of a gold shell opens the route for further functionalization of the NPs since the functionalization of gold nanoparticles and surfaces in general with DNA or thiols for example is well-known and frequently used.^{17–19} Apart from the biomedical applications that include the use of nanoparticles as contrast agents or targeted drug deliverers, other applications in high density storage devices⁴ and magneto-optical and magneto-plasmonics can be expected.^{20–22}

Hence, the fine tuning of the core and shell sizes and properties as well as the understanding of the growth mechanisms are mandatory. In their pioneer works, Xu and Wang demonstrated that Co@Au CSNPs could be generated using a gas aggregation source (or ion cluster source—ICS) with an alloyed target Co₈₀Au₂₀.^{23,24} They found that the NPs with a mean diameter of 12 nm displayed a Co core of 8 nm and a Au shell of 2 nm thickness. They argued that the formation of the CSNPs was driven by the natural diffusion of gold at the outermost part of the NPs and that the core of the nanoparticles was mainly made of cobalt, although it also contained Au atoms.

In the current work, we present a morphological, structural, and magnetic study of Co@Au NPs produced using an ion cluster source following the procedure of Xu and Wang^{23,24} but using a target with a smaller Au content (in our case Co₉₅Au₅). We show that the diffusion of gold that forms the shell and hence the thickness of the shell can be monitored by tuning the temperature of the substrate where the NPs are landing. We demonstrate that such thermal-induced diffusion allows the formation of a gold protective layer that reduces the exchange bias of NPs exposed to air even using such a low initial concentration of gold in the target material. We therefore give experimental evidence of the mechanism proposed by Xu and Wang and determine the critical temperature at which the diffusion is maximum. Note that assuming that all the gold is at the surface of a NP of 10 nm diameter the chosen chemical composition of the target would ideally lead to a core/shell Co/Au nanoparticle with a shell thickness of 0.4 nm sufficient to interfere with the EB effect. We also show that the deposition temperature has a drastic effect on the sticking coefficient (the probability that one nanoparticle that arrives at the substrate remains on it) of the NPs on naturally oxidized Si surfaces and induces crystallographic changes in the core of the NPs. Results on the magnetic properties of low and higher density deposits are presented as well.

2. RESULTS AND DISCUSSION

2.1. Morphological Characterization: AFM Results.

AFM images have been acquired to characterize the Co@Au NP deposits in terms of particle density and particle height. Although the AFM microscopy is not directly suited for the determination of the nanoparticle diameter due to the convolution of the NP contour with the AFM tip radius that results in artificially increased diameters,²⁵ it is particularly well suited for the determination of the nanoparticle height and density where there is no influence of the convolution between the tip and the measured objects. In Figure 1(a,b) we display the AFM images obtained for deposited NPs while keeping the substrates at different temperatures and deposition times. It is observed that the NPs are randomly distributed on the silicon substrates. Figure 1(a) corresponds to a 15 s deposition at RT, while Figure 1(b) corresponds to a 5 s deposition at 773 K. As can be observed the density of NPs is very similar in both cases despite the difference in deposition time (factor of 3). This

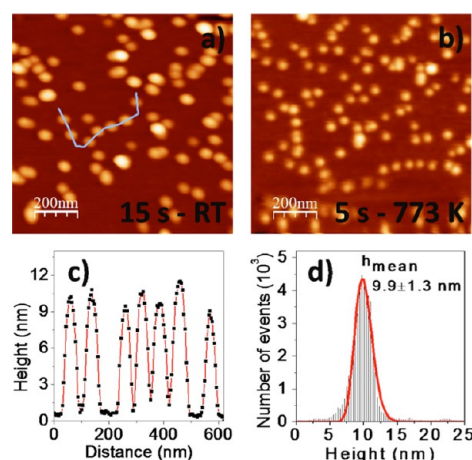


Figure 1. AFM images ($1 \mu\text{m}^2$) of Au@Co NPs deposited on Si(100) at RT (a) and 773 K (b). Deposition times were 15 and 5 s for the deposits performed at RT and 773 K, respectively. (c) Height profiles extracted from (a) where it can be seen that the height is about 10 nm. (d) Number of events versus nanoparticle height histogram extracted from the analysis of several AFM images.

clearly illustrates a NP sticking coefficient evolution with the deposition temperature that will be investigated more in depth later. Figure 1(c) illustrates the morphology of the particles as measured by AFM along the line represented in Figure 1(a), where the similar height of the NPs can be observed. The height distribution of the particles that is presented in Figure 1(d) has been extracted from several AFM images similar to those presented in Figure 1(a). It corresponds to the case of NPs deposited at RT, and the total number of events presented in the distribution is around 4600. The fit of the distribution has been performed assuming a Galton or log-normal distribution,²⁶ which among many other functions was found to best fit our distributions. The average height and standard deviation obtained from the fit were 9.9 and 1.3 nm, respectively, for all deposition temperatures.

Figures 2(a) and 2(b) display two deposits performed with the same deposition time of 15 s at RT and 773 K, respectively. This difference in the deposition temperature results in different density deposits. It should be noted that although in AFM the higher density deposits give the impression that most

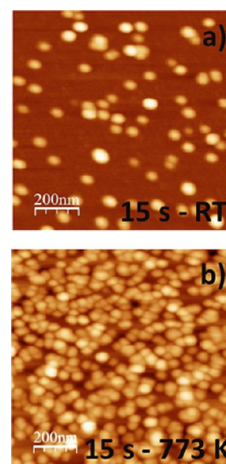


Figure 2. AFM images ($1 \mu\text{m}^2$) of Au@Co NPs deposited on Si(100) at RT (a) and 773 K (b). In both cases the deposition time was 15 s.

of the nanoparticles are in contact with each other due to the convolution effect between the AFM tip and the NPs the coverage percentage in deposits of Figure 2a and 2b is 0.9% and 3.5% of a monolayer, respectively (100% monolayer corresponds to an assembly of NPs arranged into a compact hexagonal structure on the surface). Nevertheless, the images clearly evidence that the number of deposited NPs increases with the deposition temperature, confirming a change in the sticking coefficient with the substrate temperature. In general, the sticking coefficient is associated with the energy of the NPs, the angle of incidence, the chemical nature of the surface, and its temperature. These parameters are likely to change the properties of adhesion to the substrate.²⁷ To illustrate such a phenomenon, we have represented, in Figure 3, the deposition

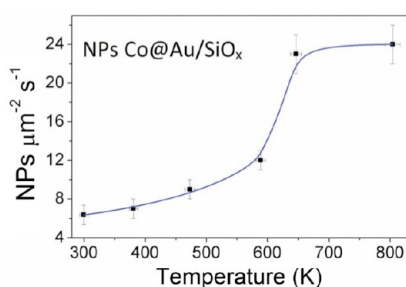


Figure 3. Deposition rate of Co@Au NPs as a function of deposition temperature.

rate (expressed as the number of deposited particles per unit area and unit time) as a function of deposition temperature. It can be observed that the deposition rate, which is proportional to the adhesion of nanoparticles on the substrate, increases with temperature up to 650 K where it stabilizes. As compared to the RT case, at the highest deposition temperature tested in this work, the deposition rate and hence the sticking coefficient have been increased by 400% approximately. Since the magnetic properties of the deposits are expected to be dependent on the density of nanoparticles,²⁸ the deposition time has been adjusted for each deposition temperature to generate low and higher density deposits. The low density deposits (LDs) correspond to an assembly of individual NPs, while in the higher density deposits (HDs) NPs are expected to interact with each other.

As discussed above, although the AFM is well suited for the measurements of height and density of NPs, it is not a precise technique to directly determine the diameter of the particles due to the convolution of the tip with the measured objects. On the other hand, TEM is well suited for the measurement of the diameter of the NPs and their internal crystallographic and chemical structure.

2.2. Structural and Chemical Characterizations: TEM Results. Representative low-magnification bright-field TEM images from NPs deposited at RT and 773 K are displayed in Figure 4a and 4b, respectively. Both deposits have been performed with the same deposition time of 15 s. The deposition rates of NPs deposited at RT and 773 K were 117 NPs/μm² s and 65 NPs/μm² s, respectively. Compared with Figure 3, it is observed that the deposition rate is higher on amorphous carbon-coated TEM grids than on silicon wafers and hence the sticking coefficient. A decrease of the sticking coefficient of 55% on TEM grids is also observed upon increase of the temperature. Although not displayed, TEM measure-

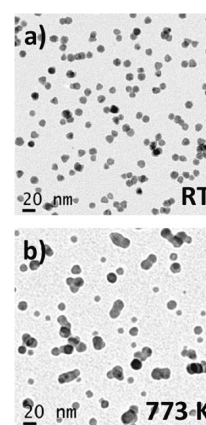


Figure 4. Low-magnification TEM images of Co@Au NPs deposited at RT (a) and 773 K (b) on TEM carbon-coated grids.

ments were also performed on deposits performed between RT and 773 K. The morphology of the cluster distribution did not exhibit marked changes up to 673 K. For temperatures above 673 K, coalescence of the NPs and the formation of bigger structures can be observed. Interestingly the coalescence of NPs was only observed on TEM grids²⁹ and not on the silicon wafer substrates. The coalescence of NPs deposited on TEM grids has been investigated and reported in previous publications. Peng and Palasantzas investigated the coalescence behavior of Co clusters. They reported that at temperatures higher than 500 K the morphology of the cluster is remarkably modified with the formation of necks between particles as a result of coalescence and growth of combined clusters.^{30,31} In our case the coalescence was not observed when the NPs were deposited on silicon wafer substrates.

The statistical study of images obtained by TEM was performed in a similar way as for the AFM images. The average diameter was found to be 10.1 nm with a standard deviation of 1.5 nm for all deposition temperatures. Within the experimental uncertainties it appears that the average height (determined by AFM) and average diameter (determined by TEM) are equal. This result shows that the spherical NPs are soft landing on the surfaces with no deformation. We have also investigated the crystalline structure of Co@Au NPs as a function of deposition temperature. In general, the crystalline structure of nanostructures is very sensitive to electron beam irradiation in TEM, and this is also the case for the Co@Au NPs. To avoid electron beam induced damage or modification of crystal structure, electron beams of low electron density and short exposures have been used. The crystal structure of the nanoparticles is obtained after the fast fourier transforms (FFTs) of high-resolution images. The theoretical interplanar distances together with the experimental ones extracted from high-resolution images are summarized in Table 1.³² The majority of the nanoparticles is polycrystalline, making the crystal structure identification difficult due to the small size of the grains causing loss of interplanar angle information in many grains of the NPs. The results presented in Table 1 are the result of a great number of FFT measurements along the NP grains. The last is illustrated in Figure 5 where we display the HRTEM images together with the FFTs. Figure 5(a) corresponds to the HRTEM image of RT deposited Co@Au NPs. For this deposition temperature, the structure was found to be purely face centered cubic (fcc). The image is characterized by the Co(111) fcc lattice fringes, and the ring distribution of the

Table 1. Theoretical and Experimental Interplanar Distances

| Co fcc | | | Co hcp | | | Au fcc | |
|--------------|-------------|---------|--------------|------------------|---------|-------------|---------|
| experimental | theoretical | | experimental | theoretical | | theoretical | |
| d (Å) | (hkl) | d (Å) | d (Å) | (hkl) | d (Å) | (hkl) | d (Å) |
| 2.05 (1) | (111) | 2.05 | 2.16 (2) | (01 $\bar{1}$ 0) | 2.17 | (111) | 2.35 |
| 1.76 (2) | (200) | 1.77 | 2.03 (1) | (0002) | 2.03 | (200) | 2.04 |
| | | | 1.92 (2) | (01 $\bar{1}$ 1) | 1.92 | | |

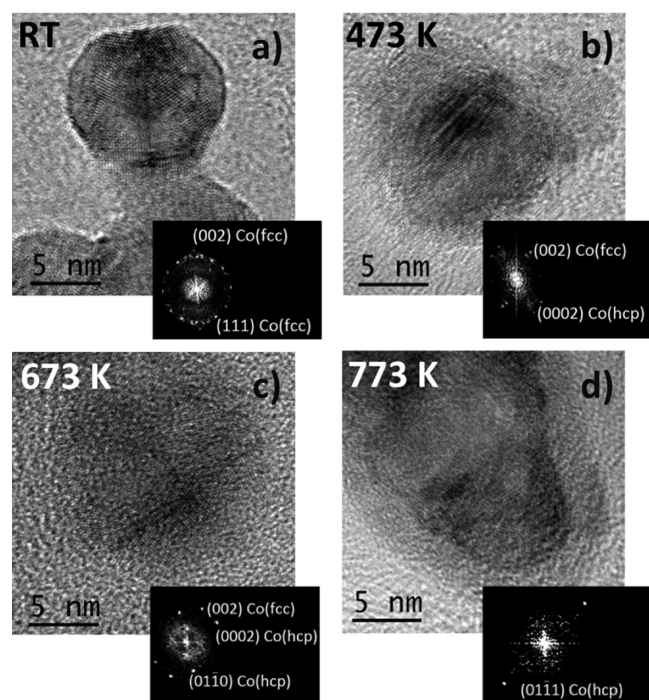


Figure 5. HRTEM images of Co@Au NPs and their corresponding FFT for different deposition temperatures: at RT (a), 473 K (b), 673 K (c), and 773 K (d).

spots observed in the FFT is consistent with a first stage of order of an icosahedral NP. Interestingly, it was found that for higher deposition temperatures hexagonal close packed (hcp) planes developed as shown in Figure 5(b–d). Previous works on Co NPs have demonstrated that the fcc structure is very stable up to a particle size of 20 nm and that a crystalline phase change would require high activation energy.³³ In our case, the observed change from fcc to hcp structures could be linked to the formation of defects/dislocations with increasing temperature and distortion of the fcc planes.³⁴ Another source of defects/dislocations could be the strain induced by Au diffusion in the NPs,²³ which seems to be stimulated by increasing the deposition temperature. However, the small amount of gold in the sputtering target (5%) and hence in the NPs does not allow the determination of the crystalline structure of gold into the NPs. On the other hand, the interplanar distances for fcc Co(111) and Au(002) planes are very similar (see Table 1), making the distinction impossible within the experimental resolution, as isolated Au grains were not observed. Structural transformations of Co particles are particularly important for magnetic properties because the coercivity is expected to increase with the volume fraction of the hcp phase.³⁴ This will be discussed in the next section.

Figures 6(a) and 7(a) display representative C_s (spherical aberration) corrected STEM-HAADF images of Co@Au NPs

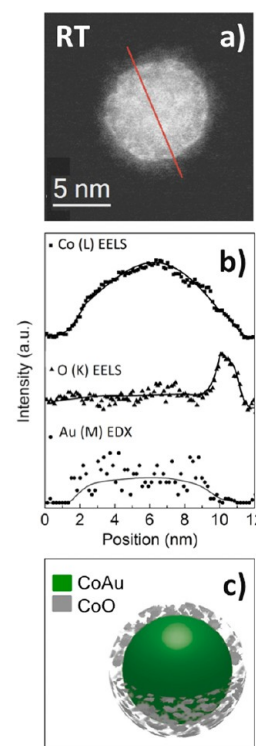


Figure 6. (a) C_s corrected STEM-HAADF image of a representative Co@Au NP deposited at RT. The line across the particle indicates the path of the electron beam where the EELS and EDX analysis of (b) have been performed. (b) The concentrations of Co, Au, and O along the scan depicted in (a). (c) Scheme of the chemical structure of the NP deposited at RT.

deposited at RT and 573 K. In both cases it can be observed that the NPs are formed by a bright core surrounded by shells that are less shiny. In STEM-HAADF Z-contrast images, lighter atoms appear darker thanks to the fact that the contrast of the images depends on Z^n (n has a value close to 2), which makes possible the identification of the elements on the materials based only on their difference in atomic number.³⁵ At a first glance, it is observed that the shell of NPs deposited at RT (Figure 6a) is incomplete, while the shell of NPs deposited at higher temperature (Figure 7a) is relatively compact. Energy-dispersive X-ray spectroscopy (EDS) and electron energy loss spectroscopy (EELS) performed along the line (electron beam path) depicted in Figure 6(a) are displayed in Figure 6(b). The chemical analysis of the NP presented in Figure 6(b) confirms such structure of the NP. While the chemical scans over the nanoparticle clearly show that both Au and Co atoms are homogeneously distributed into the NP, the scan performed on the O K edge displays an asymmetric shape. The homogeneous distribution of the Co and Au atoms into the nanoparticle indicates the formation of an alloyed core, while the asymmetric distribution of the O atoms indicates the formation of an

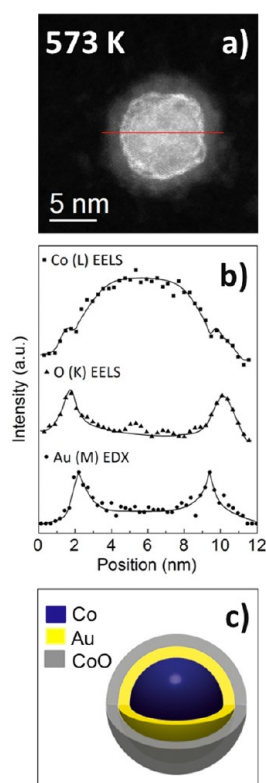


Figure 7. (a) C_s corrected STEM-HAADF of a representative Co@Au NP deposited at 573 K. The line across the particle indicates the path of the electron beam where the EELS and EDX analysis of (b) have been performed. (b) Concentrations of Co, Au, and O along the scan depicted in (a). (c) Scheme of the chemical structure of the NP deposited at 573 K.

incomplete shell of cobalt oxide. Such a chemical structure is schematically represented in Figure 6(c). The same chemical analysis has been performed on the NPs deposited at higher temperatures. The results correspondent to NPs deposited at 573 K are displayed in Figure 7(b). EDS and EELS scans reveal that the cobalt atoms are uniformly distributed in the core of the particle, while the gold atoms have migrated to the surface of this core forming a shell. Diffusion of atoms happens at elevated temperature during the particle growth. Au atoms segregate at the surface of the nanoparticles to lower the total energy of the nanoparticles. Au has a substantially lower surface energy of its (111), (100), and (110) planes, 1.61, 1.71, and 1.79 J/m², respectively, than the 2.74 J/m² of the (001) plane of Co, which is the plane of lowest surface energy of Co.^{24,36} Like in the case of RT deposition, the NP is surrounded by a cobalt oxide shell. In opposition to the RT case, the higher deposition temperature induces the formation of a continuous and thicker cobalt oxide shell. It has been also observed that the thickness of the Au and cobalt oxide shells is not constant. The thicker Au shell was found to be 1 nm and in some cases was found to be incomplete, while the average thickness of the cobalt oxide was found to be 2.5 nm. It should be noted that the origin of the oxygen that induces the formation of cobalt oxide is unknown. While for RT deposition no oxygen contamination is expected until the samples are transferred to the atmosphere, for higher deposition temperature, the presence of residual oxygen at a consequence of the outgassing of hot surfaces is possible. The origin of oxygen as well as its influence on the segregation of gold is a matter for future

investigations. The chemical structure of the NPs deposited at high temperature is schematically depicted in Figure 7(c). In this section, clear evidence of the influence of deposition temperature on the crystallographic and chemical structures of the Co@Au NPs has been presented. We will present in the next section the corresponding investigation on the magnetic properties.

2.3. Magnetic Characterization: SQUID Results. The field-cooled (FC) and zero-field-cooled (ZFC) hysteresis loops normalized to the saturation magnetization and measured at 10 K for Co@Au NPs deposited at RT and 773 K are displayed in Figure 8. Figures 8(a) and (c) correspond to low density (LD)

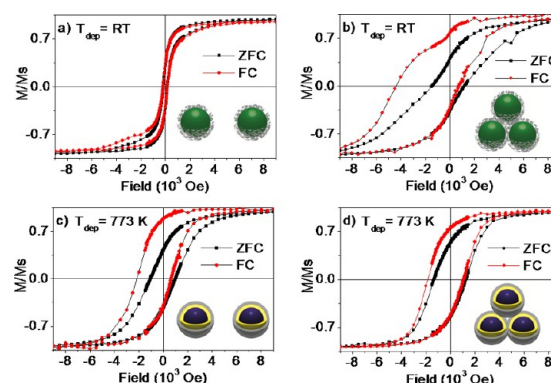


Figure 8. FC and ZFC hysteresis loops measured at 10 K for Co@Au NPs deposited at RT (a) and (b) and 773 K (c) and (d). Hysteresis loops of (a) and (c) correspond to low density deposits (LD), while hysteresis loops of figures (b) and (d) correspond to higher density deposits (HD).

deposits (0.9% of a nanoparticle monolayer) and Figures 8(b) and (d) to higher density (HD) deposits (3.5% of a nanoparticle monolayer). In both cases and in general for all deposits, the NPs displayed a ferromagnetic behavior. Note that the mean height and diameter of the nanoparticles (9.9 and 10.1 nm obtained by AFM and TEM, respectively) are very close to the superparamagnetic limit of 9 nm reported for pure monocrystalline cobalt nanoparticles.³⁷ Despite such proximity to the superparamagnetic limit and that the nanoparticles contain 5% of gold and are polycrystalline, they still display a ferromagnetic behavior. Such magnetic behavior is likely to indicate that, in a first approximation, the superparamagnetic limit does not depend strongly on the polycrystalline structure of these particles for the size of the particles investigated here. In the present paper we do not intend to perform a systematic study of the interactions as a function of density of nanoparticles.²⁸ We only compare two systems with low (LD) and high density (HD) of nanoparticles to highlight the importance of the magnetic interactions on the overall magnetic properties of the assemblies of nanoparticles. The chosen coverage for high density deposits (3.5%) corresponds to the threshold coverage reported recently for an assembly of cobalt nanoparticles of mean diameter 10 nm.²⁸

Most of the FC/ZFC hysteresis loops displayed in Figure 8 show a clear shift evidencing the presence of exchange bias (EB) effect. However, for the case of LD deposits at RT the observed EB is close to zero (Figure 8a), probably due to the small amount of antiferromagnetic (AF) cobalt oxide that is surrounding the ferromagnetic (FM) NP core.^{38–40} In that case the AF and FM volumes are not fulfilling the conditions for the development of a clear and intense EB effect.^{41,42} As presented

and discussed previously (Figures 6 and 7), the volume of cobalt oxide increases with deposition temperature (the volume of cobalt oxide is increased by a factor of 2.6 when comparing the NPs deposited at RT and higher temperature). This increase of the AF volume allows the development of the EB effect^{40,43} observed in Figure 8(c). Similar behavior of the EB has been reported on progressively oxidized Co NPs.^{40,43} The authors reported an increase of both the EB and coercive field upon oxidation of 50% of the NPs and for further oxidation a drop of both EB and coercive field (H_c). Such behavior is similar to the one reported here in the case of LD deposits as can be observed in Figures 9 and 10 where we display the

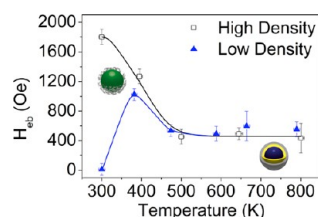


Figure 9. Evolution of the exchange bias of NPs Co@Au as a function of deposition temperature for low density (LD) and higher density (HD).

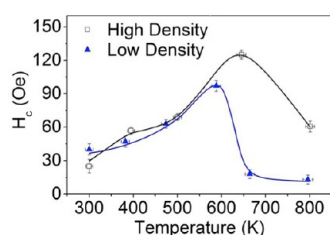


Figure 10. Evolution of the coercive field at RT as a function of deposition temperature for low density (LD) and higher density (HD).

evolution of the EB and coercive fields. In previous studies⁴⁰ the authors also reported vanishing EB and coercive fields that they ascribed to the complete oxidation of the nanoparticles that in our case is not reached due to the intermediate gold shell. The magnitude of the exchange bias (H_{EB}) represented in Figure 10 has been determined as

$$H_{EB} = \frac{|H_c^{FC+} + H_c^{FC-}|}{2}$$

where the values of coercive field at the decreasing branches (H_c^{FC+}) and increasing branches (H_c^{FC-}) were extracted from the FC hysteresis loops measured at 10 K. In the case of low density deposits, the magnitude of the EB is close to zero for RT deposits due to the formation of incomplete and too thin cobalt oxide layer at the outermost part of the NPs. Increased deposition temperature induces the formation of a thicker and more homogeneous cobalt oxide layer that favors the appearance of the EB until the gold intermediate shell quenches partially the AF–FM coupling and hence reduces the EB magnitude.

For HD deposits (Figure 8b and d), the magnetic behavior presents some differences as compared to LD deposits. While LD deposits allow the observation of the magnetic properties of individual NPs, HD deposits are expected to magnetically behave as an assembly of interacting NPs. This can be observed

in Figure 8(b) where an EB originated from the interaction between NPs can be detected. The shorter distance between NPs leads to an interaction of the cobalt oxide of nearest neighbors inducing an artificial increase of the AF volume. Such interaction is likely to produce an AF anisotropy strong enough to generate an EB effect.⁴⁴ Such EB increase with increasing density of NPs has been already reported and explained as the result of a stronger interaction between NPs that is favored by a shorter interparticle distance.^{44,45} The shape of the FC hysteresis loop of Figure 8(b) might be attributed to the coexistence of positive and negative EB effect^{42,46} among other possible scenarios magnetically complex. The positive EB is believed to be due to AF interfacial interaction.^{42,46} For the case of the Co@Au NPs deposited at 773 K (Figure 8(d)) the hysteresis loops are similar as for the low density deposit. The increased volume of AF cobalt oxide induces the presence of EB, and no double hysteresis loop is observed.^{42,47} Interfacial interactions between AF shells are probably masked by the strength of the core–shell intraparticle AF/FM interactions. Consequently, no positive EB is observed. However, the evolution of the EB upon increasing deposition temperature and for higher density deposits (Figure 9) reveals a continuous decrease of EB magnitude. This behavior is a consequence of the diffusion of gold atoms from the core of the NPs to the surface of the core that induces the formation of the Au shell that reduces the coupling between the FM Co core and the AF cobalt oxide outer shell. Note that the EB magnitude stabilizes at around 500 K deposition temperature in both LD and HD deposits. It is argued that at this temperature a balance between the formation of the AF cobalt oxide shell, an intermediate Au shell, and Co FM core is reached, as was observed in TEM analysis in Figure 7. Hence, the evolution of both EB and H_c can be explained with two complementary mechanisms: an intraparticle EB that only appears when the cobalt oxide shell has completely surrounded the ferromagnetic core and an inter or indirect EB interaction that appears when the density of nanoparticles is increased.

The interaction between the NPs can be also followed through the evolution of the coercive field of hysteresis loop measured at RT (Figure 10).⁴⁴ As can be observed, in both LD and HD cases, the H_c increases upon increasing deposition temperature and reaches a maximum at around 600–650 K. Such an increase can be ascribed to the growing portion of the Co hcp phase in comparison to the fcc phase^{34,48} in agreement with the structural results presented above and previous studies.³⁴ Such an increase can be directly related to the anisotropy constant K in the two different phases ($K_{Co_{hcp}} = 4.5 \times 10^6$ erg/cm³, $K_{Co_{fcc}} = 2.5 \times 10^6$ erg/cm³).⁴⁸ Like the evolution of the EB, the initial increase followed by a decrease of H_c as a function of deposition temperature can be explained in the frame of a progressive oxidation of the NPs and hence formation of the AF shell as reported in previous studies.^{40,43} Also the higher H_c observed for HD deposits as compared with LD deposits can be explained in the frame of interacting NPs as already reported previously.^{44,45}

3. CONCLUSIONS

We have presented a detailed morphological, structural, chemical, and magnetic study on Co@Au NPs grown using an ICS and deposited on substrates at different temperatures. We show that the deposition temperature has a drastic effect on the structure and properties of the NP systems. Upon increasing temperature, the sticking coefficient of the NPs on

silicon substrates is enhanced, and the NPs suffer a progressive change of their crystalline structure from fcc to hcp. The formation of a cobalt oxide shell is observed at all temperatures. However, such a shell is better defined at high deposition temperatures. Such chemical and structural temperature-induced modifications have an important impact on the magnetic properties of the NPs. For low density deposits, the EB effect is almost zero, while in higher density deposits, the interaction between AF shells of neighboring NPs allows the appearance of EB. The diffusion of Au atoms leads to the formation of an intermediate Au shell that protects the Co core from oxidation and reduces the AF–FM coupling, inducing a decrease of the EB effect. The formation of this Au intermediate shell has been found to be completed at a threshold temperature of 500 K where the EB effect is stabilized. In summary we have shown that thermal-induced diffusion can be used at the nanoscale to tune the structural and magnetic properties of CoAu nanoparticles.

4. EXPERIMENTAL SECTION

The NPs were generated using an Ion Cluster Source (ICS) from Oxford Applied Research⁴⁹ connected to an Ultra High Vacuum (UHV) system with base pressure in the low 10^{-9} mbar. The 2 in. diameter magnetron of the ICS was loaded with a $\text{Co}_{95}\text{Au}_5$ target (99.95% purity) and operated typically at 50 W. During deposition, the measured pressures were in the low 10^{-3} and 10^{-5} mbar ranges at the aggregation zone and in the UHV system, respectively. Si wafers (100) p-type (B doping, $\Omega = 1\text{--}10$ Ohm cm) were used as substrate except for the samples grown for TEM measurements, where the nanoparticles were deposited directly on TEM carbon-coated grids. The substrate temperature was varied from room temperature (RT) to 773 K in steps of 100 K. Two series of samples were fabricated: in the first one, the deposition time was kept constant (15 s), while in the second one, the deposition time was varied to obtain the same density of deposit. Before each deposition a degassing of the substrate was performed for 30 min at a higher temperature at which NPs were deposited to avoid further degassing and contamination of the nanoparticles during deposition.

The AFM data were acquired using the Cervantes AFM System equipped with the “Dulcinea” electronics from Nanotec Electrónica S.L.⁵⁰ The measurements were performed in dynamic mode using commercial silicon AFM tips with a typical radius of less than 7 nm and a force constant of 42 N/m. The image analysis was made using a combination of the WSxM⁵⁰ and ImageJ⁵¹ softwares from Nanotec and the National Center for Biotechnology Information.

TEM analyses were performed in two different microscopes. Morphology and structure were investigated in the Laboratorio de microscopía electrónica de transmisión at the Universidad Carlos III de Madrid, using a Philips Tecnai 20F FEG analytical microscope, operating at 200 kV, equipped with an energy-dispersive X-ray (EDX) analysis system and a STEM modulus with an HAADF detector for Z-contrast images. Crystal structure studies were carried out by electron diffraction and electron diffraction pattern simulation, using Fast Fourier Transform (FFT) of the HRTEM images. The compositional studies were partially conducted in the Laboratorio de Microscopías Avanzadas at the Instituto de Nanociencia de Aragón - Universidad de Zaragoza, Spain. The FEI-TITAN X-FEG transmission electron microscope was used in STEM mode and operated at 300 kV. The images were acquired using

a high-angle annular dark field (HAADF) detector with the desired camera length easily satisfying the Z^2 contrast condition. In addition, the microscope is equipped with a monochromator, Gatan Energy Filter Tridien 866 ERS, and a spherical aberration corrector (CEOS) for the electron probe allowing an effective 0.08 nm spatial resolution. The column is also fitted with an EDS (EDAX) detector for EDS analysis. The analysis of TEM images was performed with the TEM Imaging and Analysis (TIA) software from FEI Company and the DigitalMicrograph from Gatan, Inc.

The magnetic measurements have been performed in a Superconducting Quantum Interference Device (SQUID) magnetometer from Quantum Design and equipped with a 5 T (50 kOe) coil. The magnetic field was applied parallel to the sample surface, and the samples were carefully demagnetized before measurements. In the case of field-cooled (FC) measurements the samples were cooled under a magnetic field of 50 kOe. The diamagnetic contribution coming from the Si substrates has been carefully measured for further subtraction from the measured data.

AUTHOR INFORMATION

Corresponding Author

*E-mail: huttel@icmm.csic.es. Tel.: +34 91 334 90 98.

Notes

The authors declare no competing financial interest.

ACKNOWLEDGMENTS

Work was supported by the Spanish Ministerio de Ciencia e Innovación under projects MAT2008-06765-C02, MAT2011-29194-C02-02, MAT2011-27470-C02-02, CSD2007-00041 (NANOSELECT), and CSD2009-00013 (IMAGINE). D. Llamasa P. acknowledges financial support from Ministerio de Ciencia e Innovación under contract n° JAEPre-09-01925. L.M. and E.R. acknowledge the Consejo Superior de Investigaciones Científicas (PIE 201160E085). The microscopy works have been partially conducted in the “Laboratorio de Microscopías Avanzadas” at “Instituto de Nanociencia de Aragón - Universidad de Zaragoza”, Spain. and also at LABMET laboratory associated to the Red de Laboratorios of Comunidad de Madrid, Spain.

REFERENCES

- (1) Kalska, B.; Fumagalli, P.; Hilgendorff, M.; Giersig, M. *Mater. Chem. Phys.* **2008**, *112*, 1129–1132.
- (2) Bansmann, J.; Baker, S. H.; Binns, C.; Blackman, J. A.; Bucher, J. P.; Dorantes-Dávila, J.; Dupuis, V.; Favre, L.; Kechrakos, D.; Kleiberg, A.; et al. *Surf. Sci. Rep.* **2005**, *56*, 189–275.
- (3) Martín, J. I.; Nogués, J.; Liu, Kai; Vicent, J. L.; Schuller, I. K. *J. Magn. Magn. Mater.* **2003**, *256*, 449–551.
- (4) Skumryev, V.; Stoyanov, S.; Zhang, Y.; Hadjipanayis, G.; Givord, D.; Nogués, J. *Nature* **2003**, *423*, 850–853.
- (5) Iglesias, O.; Batlle, X.; Labarta, A. *J. Phys. D: Appl. Phys.* **2008**, *41*, 134010.
- (6) Givord, D.; Skumryev, V.; Nogués, J. *J. Magn. Magn. Mater.* **2005**, *294*, 111–116.
- (7) Douvalis, A. P.; Zboril, R.; Bourlinos, A. B.; Tucek, J.; Spyridi, S.; Bakas, T. *J. Nanopart. Res.* **2012**, *14*, 1130.
- (8) Martínez-Boubeta, C.; Simeonidis, K.; Serantes, D.; Conde-Leborán, I.; Kazakis, I.; Stefanou, G.; Peña, L.; Galceran, R.; Lluís Balcells, L.; Monty, C.; et al. *Adv. Funct. Mater.* **2012**, *22*, 3737–3744.
- (9) Salazar-Alvarez, G.; Sort, J.; Suriñach, S.; Dolors Baró, M.; Nogués, J. *J. Am. Chem. Soc.* **2007**, *129*, 9102–9108.

- (10) Lu, X.; Liang, G.; Sun, Z.; Zhang, W. *Mater. Sci. Eng. B* **2005**, *117*, 147–152.
- (11) Cao, C.; Ma, Z.; Ma, C.; Pan, W.; Liu, Q.; Wang, J. *Mater. Lett.* **2012**, *88*, 61–64.
- (12) Trunova, A. V.; Lindner, J.; Meckenstock, R.; Spasova, M.; Farle, M.; Ciuculescu, D.; Amiens, C.; Chaudret, B.; Respaud, M. *J. Magn. Magn. Mater.* **2009**, *321*, 3502–3506.
- (13) Liu, H.; Hou, P.; Zhang, W.; Wu, J. *Colloids Surf., A* **2010**, *356*, 21–27.
- (14) Song, A.-Y.; Wu, J. H.; Min, J. H.; Tan, R. P.; Lee, J. S.; Kim, Y. K. *IEEE Trans. Magn.* **2009**, *45*, 4041–4044.
- (15) Park, J.-I.; Kim, M. G.; Jun, Y.-W.; Lee, J. S.; Lee, W.-R.; Cheon, J. *J. Am. Chem. Soc.* **2004**, *126*, 9072–9078.
- (16) Chen, M.; Yamamuro, S.; Farrell, D.; Majetich, S. A. *J. Appl. Phys.* **2003**, *93*, 7551–7553.
- (17) DeLong, R. K.; Reynolds, C. M.; Malcolm, Y.; Schaeffer, A.; Severs, T.; Wanekaya, A. *J. Nanotechnol., Sci. Appl.* **2010**, *3*, 53–63.
- (18) Mariscal, M. M.; Olmos-Asar, J. A.; Gutierrez-Wing, C.; Mayoral, A.; Yacaman, M. J. *Phys. Chem. Chem. Phys.* **2010**, *12*, 11785–11790.
- (19) Martínez, L.; Carrascosa, L. G.; Hüttel, Y.; Lechuga, L. M.; Román, E. *Phys. Chem. Chem. Phys.* **2010**, *12*, 3301–3308.
- (20) Smolensky, E. D.; Neary, M. C.; Zhou, Y.; Berquo, T. S.; Pierre, V. C. *Chem. Commun.* **2011**, *47*, 2149–2151.
- (21) Essone Mezeme, M.; Lasquelle, S.; Brosseau, C. *J. Appl. Phys.* **2011**, *109*, 014302.
- (22) Bao, Y.; Calderon, H.; Krishnan, K. M. *J. Phys. Chem. C* **2007**, *111*, 1941–1944.
- (23) Xu, Y. H.; Wang, J. P. *IEEE Trans. Magn.* **2007**, *43*, 3109–3111.
- (24) Xu, Y. H.; Wang, J. P. *Adv. Mater.* **2008**, *20*, 994–999.
- (25) Martínez, L.; Tello, M.; Díaz, M.; Román, E.; Garcia, R.; Hüttel, Y. *Rev. Sci. Instrum.* **2011**, *82*, 023710.
- (26) Ogrady, K.; Bradbury, A. *J. Magn. Magn. Mater.* **1983**, *39*, 91–94.
- (27) Nakagawa, K.; Yamaguchi, S.; Sugii, N.; Shiraki, Y. *Mater. Sci. Eng. B* **2002**, *89*, 238–140.
- (28) Ruano, M. M.; Díaz, M.; Martínez, L.; Navarro, E.; Román, E.; García-Hernandez, M.; Espinosa, A.; Ballesteros, C.; Fermento, R.; Hüttel, Y. *Phys. Chem. Chem. Phys.* **2013**, *15*, 316–329.
- (29) Mayoral, A.; Mejia-Rosales, S.; Mariscal, M. M.; Perez-Tijerín, E.; Jose-Yacaman, E. *Nanoscale* **2010**, *2*, 2647–2651.
- (30) Peng, D. L.; Konno, T. J.; Wakoh, K.; Hihara, T.; Sumiyama, K. *Appl. Phys. Lett.* **2001**, *78*, 1535–1537.
- (31) Palasantzas, G.; Vystavel, T.; Koch, S. A.; De Hosson, J.; Th, M. *J. Appl. Phys.* **2006**, *99*, 024307.
- (32) Wyckoff, R. W. G. In *Crystal Structures*, 2nd ed.; Interscience: New York, 1964; Vol. 2.
- (33) Kitakami, O.; Sato, H.; Shimada, Y. *Phys. Rev. B* **1997**, *56*, 13849–13854.
- (34) Sato, H.; Kitakami, O.; Sakurai, T.; Shimada, Y.; Otani, Y.; Fukamichi, K. *J. Appl. Phys.* **1997**, *81*, 1858–1862.
- (35) Mayoral, A.; Leonard Deepak, F.; Esparza, R.; Casillas, G.; Magen, C.; Perez-Tijerín, E.; Jose-Yacaman, M. *Micron* **2012**, *43*, 557–564.
- (36) Skriver, H. L.; Rosengaard, N. M. *Phys. Rev. B* **1992**, *46*, 7157–7168.
- (37) De Toro, J. A.; Andrés, J. P.; González, J. A.; Muñoz, P.; Riveiro, J. M. *Nanotechnology* **2009**, *20*, 085710.
- (38) Jungblut, R.; Coehoorn, R.; Johnson, M. T.; de Stegge, J. A.; Reinders, A. *J. Appl. Phys.* **1994**, *75*, 6659–6664.
- (39) Ali, M.; Adie, P.; DMarrows, C. H.; Greig, D.; Hickey, B. J.; Stamps, R. L. *Nat. Mater.* **2007**, *6*, 70–75.
- (40) Kovylyna, M.; García del Muro, M.; Konstantinović, Z.; Varela, M.; Iglesias, O.; Labarta, A.; Batlle, X. *Nanotechnology* **2009**, *20*, 175702.
- (41) Nogués, J.; Schuller, I. K. *J. Magn. Magn. Mater.* **1999**, *192*, 203–232.
- (42) Nam, N. T.; Thuy, N. P.; Tuan, N. A.; Phuoc, N. N.; Suzuki, T. *J. Magn. Magn. Mater.* **2007**, *315*, 82–88.
- (43) Morel, R.; Brenac, A.; Portemont, C. *J. Appl. Phys.* **2004**, *95*, 3757–3760.
- (44) Portemont, C.; Morel, R.; Brenac, A.; Notin, L. *J. Appl. Phys.* **2006**, *100*, 033907.
- (45) Nogués, J.; Skumryev, V.; Sort, J.; Stoyanov, S.; Givord, D. *Phys. Rev. Lett.* **2006**, *97*, 157203.
- (46) Phuoc, N. N.; Thuy, N. P.; Tuan, N. A.; Le Thanh, H.; Thanh, N. T.; Nam, N. T. *J. Magn. Magn. Mater.* **2006**, *298*, 43–47.
- (47) Thuy, N. P.; Tuan, N. A.; Phuoc, N. N.; Nam, N. T.; Hien, T. D.; Hai, N. H. *J. Magn. Magn. Mater.* **2006**, *304*, 41–45.
- (48) Yang, H. T.; Su, Y. K.; Shen, C. M.; Yang, T. Z.; Gao, H. J. *Surf. Interface Anal.* **2004**, *36*, 155–160.
- (49) Oxford Applied Research, <http://www.oaresearch.co.uk/oaresearch/cluster>.
- (50) Horcas, I.; Fernandez, R.; Gomez-Rodriguez, J. M.; Colchero, J.; Gomez-Herrero, J.; Baro, A. M. *Rev. Sci. Instrum.* **2007**, *78*, 013705.
- (51) <http://rsbweb.nih.gov/ij>.